



## ISTITUTO NAZIONALE DI RICERCA METROLOGICA Repository Istituzionale

Magnetoresponse Devices with Programmable Behavior Using a Customized Commercial Stereolithographic 3D Printer

*Original*

Magnetoresponse Devices with Programmable Behavior Using a Customized Commercial Stereolithographic 3D Printer / Lantean, S; Roppolo, I; Sangermano, M; Hayoun, M; Dammak, H; Barrera, G; Tiberto, P; Pirri, Cf; Bodelot, L; Rizza, G. - In: ADVANCED MATERIALS TECHNOLOGIES. - ISSN 2365-709X. - 7:11(2022), p. 2200288. [10.1002/admt.202200288]

*Availability:*

This version is available at: 11696/75945 since: 2023-02-21T13:14:57Z

*Publisher:*

WILEY

*Published*

DOI:10.1002/admt.202200288

*Terms of use:*

This article is made available under terms and conditions as specified in the corresponding bibliographic description in the repository

*Publisher copyright*

(Article begins on next page)

# Magneto-responsive Devices with Programmable Behavior Using a Customized Commercial Stereolithographic 3D Printer

Simone Lantean, Ignazio Roppolo,\* Marco Sangermano, Marc Hayoun, Hichem Dammak, Gabriele Barrera, Paola Tiberto, Candido Fabrizio Pirri, Laurence Bodelot, and Giancarlo Rizza

The revolution of 4D printing allows combining smart materials to additive processes to create behavioral objects able to respond to external stimuli, such as temperature, light, electrical, or magnetic fields. Here, a modified commercial digital light processing (DLP) 3D printer is used to obtain complex macroscopic remotely controlled gear-based devices. The fabrication process is based on the printing of magneto-responsive polymers containing in situ self-assembled microstructures, i.e., composed of oriented chains of Fe<sub>3</sub>O<sub>4</sub> nanoparticles (NPs). First, it is demonstrated that magneto-responsive hammer-like actuators with different stiffness can be printed allowing both pure rotation or/and bending motions. Then, the microstructure to create a magneto-responsive gear is exploited. In particular, this work shows that they can be successfully used to transfer torque to other gears, thereby converting a rotation movement into linear translation. Finally, it is demonstrated that magneto-responsive gears can also be combined with other nonmagnetic elements to create complex assemblies, such as gear-trains, linear actuators, and grippers that can be remotely controlled.

number of architectures and peculiar properties, as the ability to undergo motion in response to environmental stimuli.<sup>[1,2]</sup> For instance, in abalone shells and shrimps the oriented and hierarchical microstructure is responsible for their outstanding impact resistance,<sup>[3,4]</sup> in carnivorous plants, as the *Dionaea muscipula*, the microstructure is exploited to induce precise shape morphism, in pinecones the motion is actuated in response to humidity.<sup>[5–9]</sup> Magnetotactic bacteria synthesize magnetic iron nanominerals inside them, which function as tiny compasses allowing them to navigate by means of Earth's geomagnetic field.<sup>[10]</sup> From a technical point of view, despite the attempts to mimic and reproduce natural architectures and patterns, conventional fabrication techniques often face technical and resolution limitations. In the last years, this gap is being partially bridged thanks to the

development of the 3D printing, where starting from a computer-aided design (CAD) file, the final object is built through the additive deposition of material subunits. However, the real breakthrough in this field of research has been to first imagine

## 1. Introduction

Materials science is continuously inspired by Nature. Millions of years of evolution led living matter to develop an endless

S. Lantean, I. Roppolo, M. Sangermano, C. F. Pirri  
Department of Applied Science and Technology  
Politecnico di Torino  
Duca degli Abruzzi, 24, Torino 10124, Italy  
E-mail: ignazio.roppolo@polito.it

S. Lantean, M. Hayoun, H. Dammak, G. Rizza  
Laboratoire des Solides Irradiés (LSI)  
Institut Polytechnique de Paris  
CEA/DRF/IRAMIS  
CNRS  
École polytechnique  
Route de Saclay, Palaiseau 91128, France

© 2022 The Authors. Advanced Materials Technologies published by Wiley-VCH GmbH. This is an open access article under the terms of the Creative Commons Attribution License, which permits use, distribution and reproduction in any medium, provided the original work is properly cited.

 The ORCID identification number(s) for the author(s) of this article can be found under <https://doi.org/10.1002/admt.202200288>.

DOI: 10.1002/admt.202200288

I. Roppolo, C. F. Pirri  
Center for Sustainable Future Technologies  
Istituto Italiano di Tecnologia  
Via Livorno 60, Torino 10144, Italy

H. Dammak  
Laboratoire Structures Propriétés et Modélisation des Solides  
CentraleSupélec  
CNRS  
Université Paris-Saclay  
Gif-sur-Yvette F 91190, France

G. Barrera, P. Tiberto  
Advanced Materials for Metrology and Life Sciences Division  
INRiM Strada delle Cacce 91  
Torino 10143, Italy

L. Bodelot  
Laboratoire de Mécanique des Solides (LMS)  
CNRS  
École polytechnique  
Institut Polytechnique de Paris  
Route de Saclay, Palaiseau 91128, France

and then print behavioral objects.<sup>[11]</sup> This is the domain of the so-called 4D printing, which is, in a way, the functional form of 3D printing.<sup>[12–14]</sup> Instead of printing only static objects, it becomes possible to print functions. This paradigm shift allows a printed object to adapt to its environment and to evolve in a controlled way through the application of stimuli. So far, the 4D printing approach has been applied to functional polymers or composite materials such as hydrogels,<sup>[15–18]</sup> electroactive polymers,<sup>[19–21]</sup> shape memory polymers,<sup>[22–26]</sup> or polymers sensitive to pH,<sup>[27,28]</sup> and light.<sup>[29,30]</sup> Yet, the research on 4D printed objects with controlled microstructure is still in its infancy and it mainly focuses on the fabrication of composite materials with enhanced mechanical properties,<sup>[31–40]</sup> where only a few works mention the possibility to control the microstructure in situ during the printing process.<sup>[41–46]</sup> In particular, we are interested here in the tailor-made printing of magnetoreactive composite polymers.<sup>[47–49]</sup> Indeed, they can be easily actuated by remote magnetic fields without damaging tissues and organs, and thus be used for instance in soft robotics for healthcare and biomedical applications.<sup>[50,51]</sup> A first strategy to print magnetoresponsive composite polymers consists in using hard magnetic fillers, such as Nd<sub>2</sub>Fe<sub>14</sub>B microparticles, and to orient their permanent dipoles using external strong magnets.<sup>[52–54]</sup> This process has been mainly applied in fused filament fabrication (FFF) and direct ink writing (DIW) 3D printing techniques.<sup>[53,55]</sup> In those cases, despite the fabrication of large objects in the X–Y plane, layer-to-layer adhesion issues generally limit their thickness to a few hundred microns.<sup>[55]</sup> Furthermore, the use of such microparticles can be problematic in light-activated 3D printing (stereolithography and digital light processing (DLP)) due to an increase in viscosity and to light scattering, which can affect the printing procedure.<sup>[56]</sup> A second strategy exploits the self-assembly of soft magnetic fillers, such as Fe<sub>3</sub>O<sub>4</sub> nanoparticles (NPs).<sup>[57–59]</sup> Magnetite is a low cost and earth-abundant material, available commercially in many forms, including NPs. When soft magnetic fillers are dispersed within a liquid medium and exposed to an external field, they spontaneously assemble into chain-like filamentary structures aligned along the field vector. The dimension and direction of the assembled chains, i.e., the microstructure, can be programmed by varying the experimental parameters such as the intensity of the applied magnetic field, the NPs concentration, and the viscosity of the medium.<sup>[60–62]</sup> The microstructure can be rapidly frozen by curing the formulation, embedding it in a matrix.<sup>[60–62]</sup> This creates a uniaxial magnetic anisotropy characterized by a magnetic easy axis (i.e., the major axis of the chains) along which the magnetic moments of single NPs are preferentially oriented, thereby forming an extended magnetic dipole in the chain.<sup>[61–63]</sup> This is particularly advantageous in light-activated technologies, and it can be exploited to actuate the printed object. Indeed, if an angle exists between the applied external magnetic field and the magnetic easy axis of the chains, a torque is exerted, which forces the object to rotate to align itself along the field vector.<sup>[63–65]</sup> Therefore, controlling the orientation of the magnetic microstructure allows programming the rotation and bending movements of the printed objects. So far, this approach has been mainly employed in 2D fabrication processes,<sup>[66–69]</sup> in particular using a photolithographic approach, with the fabrication of multimodal microactuators.<sup>[70]</sup>

More recently, the self-assembly process has also been applied to control the microstructure of twist-type microswimmers fabricated by direct laser writing and actuated by external rotating fields,<sup>[71–75]</sup> or to fabricate cellularized magnetoresponsive hybrid hydrogels using a 3D bio-printing technique.<sup>[76]</sup>

The present work is based on the knowledge we developed so far in the formulation of photocurable magnetoactive acrylic resins,<sup>[77]</sup> as well as the in situ control of the self-assembly of magnetite (Fe<sub>3</sub>O<sub>4</sub>) NPs during the printing process.<sup>[78]</sup> Here, our erstwhile knowledge is exploited to create macroscopic complex assemblies of magnetodrive elements, that can be remotely controlled. This is done in three steps: first, the formation of a controlled microstructure through the self-assembly of Fe<sub>3</sub>O<sub>4</sub> NPs dispersed in photocurable resin as well as its spatial orientation have been investigated and rationalized by using numerical simulations. Second, we modified a commercial DLP printer<sup>[78]</sup> to obtain complex magnetoresponsive objects, whose magnetic and mechanical properties have been measured for different formulations of the resin, different overall contents of magnetic fillers, and different spatial orientations of the microstructure. Finally, as a proof-of-concept, we fabricated different magnetoresponsive devices: hammer-like actuators with different stiffnesses, as well as magnetoresponsive gears. Additionally, we combined magnetoresponsive components with nonmagnetic elements to create complex assemblies, such as gear-trains, linear actuators, and grippers that can be remotely controlled.

## 2. Result and Discussion

The optimum condition to print magnetoresponsive composite materials depends on three parameters: i) the average length of the self-assembled chains, ii) their spatial orientation, and iii) the concentration of the loaded magnetic fillers.<sup>[78]</sup> Figure S1 (Supporting Information) illustrates the time evolution of the average length of self-assembled chains when exposed to a magnetic field of 10 mT. Here, the timeframe is limited to 180 s to be compatible with the printing process, and each point represents the average of at least 200 measurements. For both formulations, the chains' length reaches a plateau within 180 s; however, their values are quite different. Indeed, the formulation having the lower viscosity (50Eb50BA and open circles) leads to the formation of chains that are more than twice as long, i.e., ≈50 μm, than those formed in the more viscous formulation (75Eb25BA and full circles), i.e., ≈20 μm.

Once the chains of magnetic fillers have reached their saturation length, the microstructure can be spatially oriented by rotating the magnetic field. In this case, the aggregates will be submitted to a torque that will force the chains to reorient their magnetic dipoles along the direction of the applied field,<sup>[62,79–83]</sup> see Figure S1 (Supporting Information), for the 50Eb50BA formulation. First, the self-assembly is triggered along  $\theta_B = 0$ , i.e., the horizontal direction, Figure S1d (Supporting Information). Then, to mimic the spatial orientation of the microstructure during the printing process, the magnetic field is rotated by  $\theta_B = 30^\circ$ , Figure S1e (Supporting Information). In both cases, the numerical simulations correctly describe the dynamic evolution of the chains. After preliminary investigations on microscope slides, the formulations were tested for

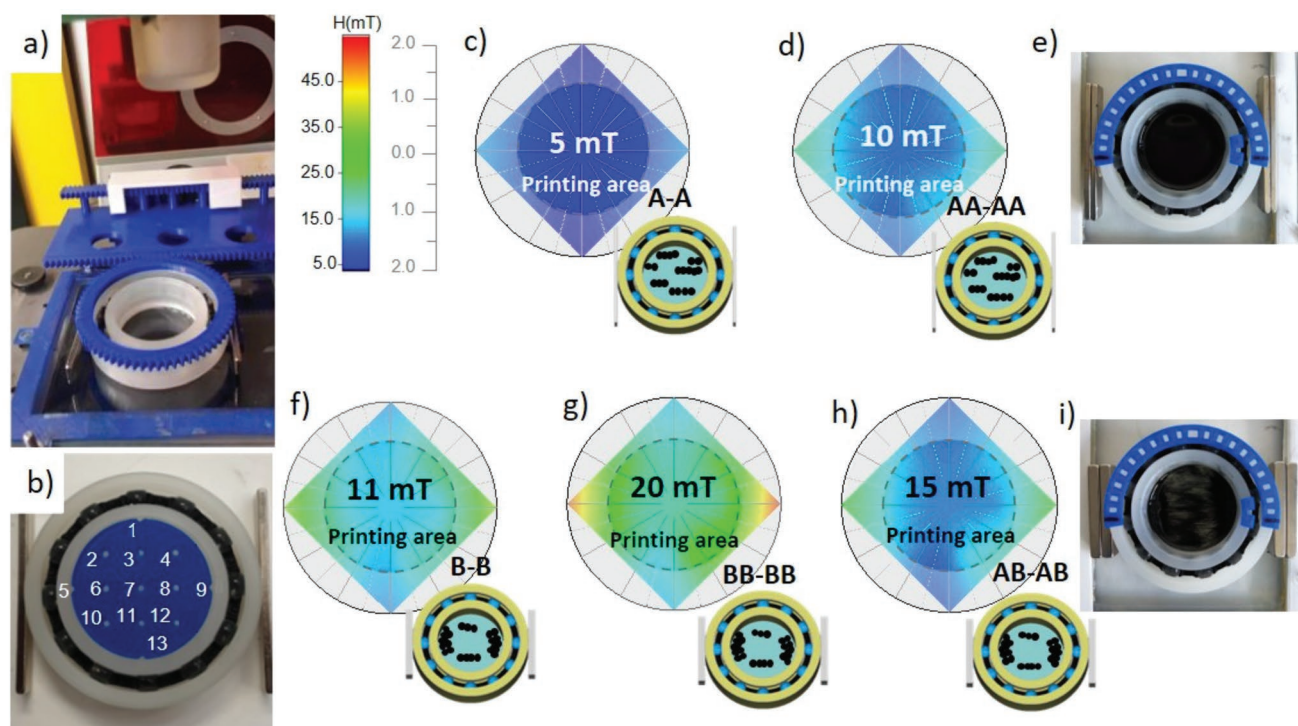


**Figure 1.** a) Modified digital light processing (DLP) printer. b) Experimental mapping of the magnetic field distribution within the vat for several combinations of permanent magnets, named as A and B. A magnets are  $60 \times 10 \times 2 \text{ mm}^3$  parallelepipeds exhibiting a magnetic field at the surface of 120 mT, while B magnets are  $40 \times 10 \times 4 \text{ mm}^3$  parallelepipeds exhibiting a magnetic field at the surface of 310 mT. c) A-A and d) AA-AA configurations present e) a homogeneous distribution of the magnetic fillers dispersed within the photocurable resin. In contrast, for f) B-B, g) BB-BB, and h) BA-AB configurations, i) inhomogeneities as well as depleted areas are observed in the vat.

additive process on the modified DLP 3D printer. The necessary condition for obtaining objects with uniform magnetic properties is that the distribution of magnetic fillers inside the resin vat remains homogeneous throughout the printing process. Thus, the applied magnetic field has been first mapped by measuring its value in 13 different zones of the printing area as shown in **Figure 1b**. Then, the stability of the NPs distribution was tested for at least 30 min, a time compatible with the duration of the fabrication of a 5 mm thick object. Configurations composed of A-A and AA-AA magnets produce quasi-homogeneous magnetic field distributions with an intensity at the center of the printing area of 5 mT and 10 mT, respectively, and a gradient of about  $\delta G_x = 1 \div 2 \text{ mT cm}^{-1}$  (**Figure 1c,d**). In both cases, a homogeneous distribution of the NPs within the printing area is observed as shown in **Figure 1e**. In contrast, for the B-B, BB-BB, and BA-AB configurations (**Figure 1f-h**)—producing a magnetic field at the center of the printing area of 11, 20, and 15 mT, respectively, and a field gradient of about  $\delta G_x = 5 \div 10 \text{ mT cm}^{-1}$ —the migration of the fillers toward the edges of the ball bearing as well as the formation of a depleted central zone are observed, **Figure 1i**. As the depletion process is driven by the gradient of the magnetic field,<sup>[84]</sup> a value of  $\delta G_x \approx 1 \div 2 \text{ mT.cm}^{-1}$  has been chosen as the upper threshold guaranteeing the homogeneous spatial distribution of the fillers during the printing step. In particular, the AA-AA configuration gives the optimum conditions to print magneto-responsive elements containing homogeneously distributed spatially oriented microstructures.

The next step was the optimization of the processing parameters for the used formulations reported in **Table 1**. As expected, the curing time (i.e., the time necessary to cure a single layer) increases with the NPs concentration, while it is only slightly influenced by the concentration of butyl acrylate (BA).<sup>[77]</sup> On the other hand, the printing parameters are not modified by the applied magnetic field used to create the microstructure.

Field emission scanning electron microscopy (FESEM) was used to verify both the efficiency of the self-assembly process during the 3D printing phase and the incorporation of the magnetic chains within the polymer matrix. **Figure 2a1-c 1** shows

**Table 1.** Printing parameters used to 3D print the magneto composite polymers.

Sample	Alignment magnetic field [mT]	Slicing [ $\mu\text{m}$ ]	Base exposing time [s]	Object exposing time [s]	
75Eb25BA_2wt%NPs	0	10	20	2.9	1.6
75Eb25BA_4wt%NPs	0	10	20	4.4	2
75Eb25BA_6wt%NPs	0	10	20	5.8	2.4
75Eb25BA_8wt%NPs	0	10	20	9.5	3
50Eb50BA_2wt%NPs	0	10	20	2.9	1.4
50Eb50BA_4wt%NPs	0	10	20	4.2	1.8
50Eb50BA_6wt%NPs	0	10	20	5.5	2.2
50Eb50BA_8wt%NPs	0	10	20	9.5	3

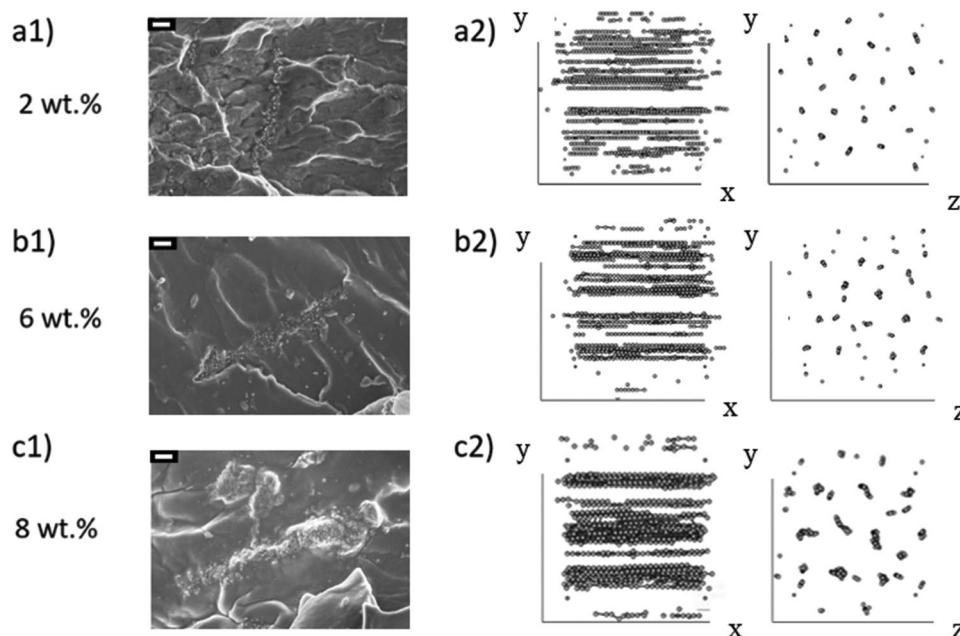


**Figure 2.** Field emission scanning electron microscopy (FESEM) cross-section images of 3D printed 75Eb25BA samples with increasing content of magnetic fillers: a1) 2 wt%, b1) 6 wt%, c1) 8 wt%. The scale bar is 20  $\mu\text{m}$ . a2–c2) Numerical simulations based on a dipolar approximation model.

that chains of magnetic fillers are systematically observed in each prepared sample. In addition, not only their length but also their width increases with the volume fraction of the embedded NPs with a subsequent effect on the aspect ratio of the chains. These results are confirmed by the numerical simulations (Figure 2a2–c2) and can be easily understood by considering that the interparticle distance decreases with increasing their load.<sup>[85]</sup> Thus, NPs are more likely to interact and yield larger assembled structures in highly loaded systems than in dilute ones.

Finally, the printability of complex objects as well as the fidelity to the original CAD file have been validated for the 75Eb25BA and 50Eb50BA formulations containing 6 wt% of magnetic fillers, by printing an Archimede's screw containing a microstructure spatially oriented by rotating the applied magnetic field (10 mT) by  $\theta_B = 30^\circ$  every 20 printed layers,

i.e., 400  $\mu\text{m}$  of the printed object (Figure 3). In Figure 3, the original STL file (Figure 3a) and the printed object (Figure 3b) are shown together with a heat map (Figure 3c) reporting the differences between the digital file and the digitalization of the real object created by 3D scanning. As can be observed, the fidelity is very good (standard deviation 0.022  $\mu\text{m}$ , average error about 100  $\mu\text{m}$ ).

The magnetic properties of a 3D printed object containing an oriented microstructure were investigated on a  $3 \times 3 \times 3$  mm cubic specimen, as reported in Figure 4a. The magnetic behavior of the sample containing 6 wt% of  $\text{Fe}_3\text{O}_4$  NPs (shown in Figure 4b–e) is representative of all the synthesized composites loaded with different NPs concentrations. Figure 4b shows the sample containing a random dispersion of magnetic fillers. It is characterized by a perfect overlap of the hysteresis loops measured along the  $x$ ,  $y$ , and  $z$  axes, which in turn results in

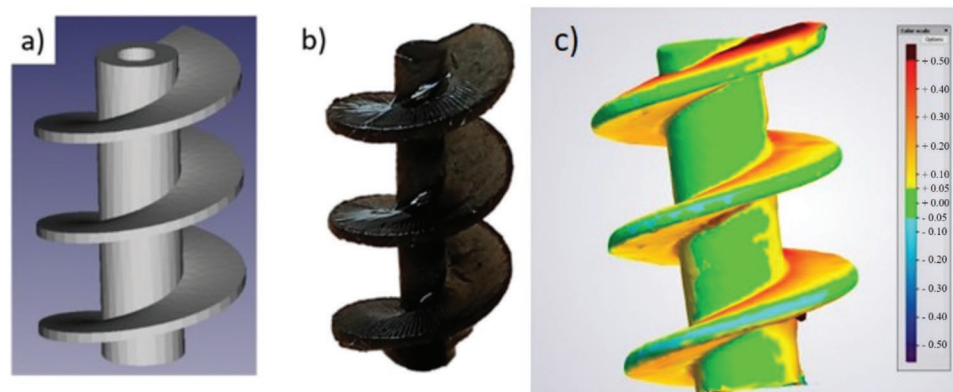


**Figure 3.** a) Computer-aided design (CAD) file of an Archimede's screw used to check the feasibility and the fidelity of the printing process. b) Image of the printed object containing a spatially oriented microstructure. c) Heat map reporting the differences between the original STL file and the digitalization of the 3D printed object obtained by 3D scanning.

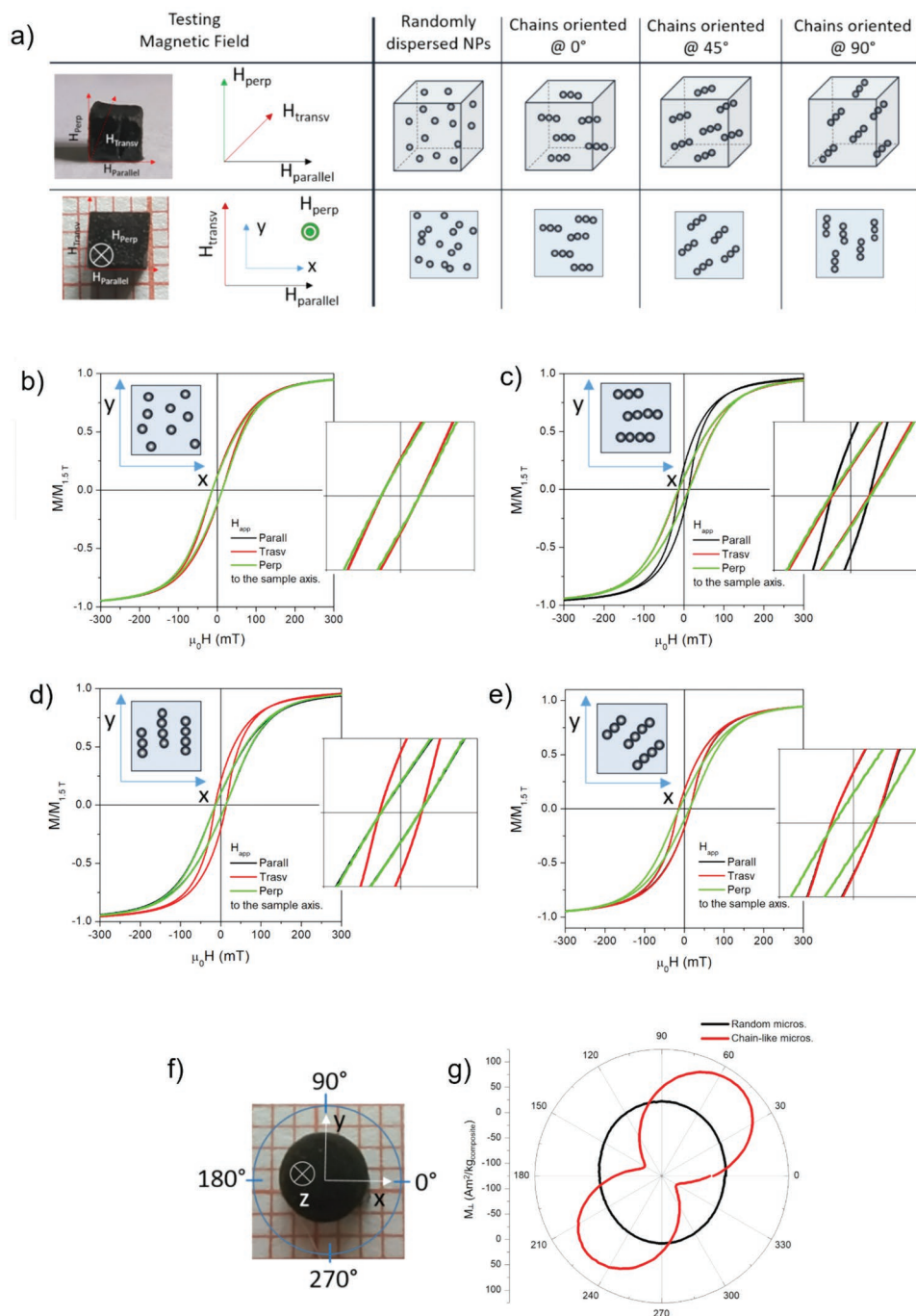


**Figure 4.** a) Sketch of configuration used to measure the magnetic response of a 3D printed cube. Two configurations have been probed: randomly dispersed nanoparticles (NPs), and chains of NPs aligned along x-direction (0°), y-direction (90°) and at 45°. Magnetic hysteresis loops measured along the x (black line), y (red line) and z (green line) directions for the 75Eb25BA\_6NPs samples differing by their microstructure: b) randomly dispersed NPs, c) chains oriented at 0°, d) chains oriented at 45°, e) chains oriented at 90°. f) 3D printed cylinder used to measure the angular dependence of the magnetic anisotropy. g) Polar plots for the perpendicular ( $M_{\perp}$ ) component of the magnetization; black curve:  $\text{Fe}_3\text{O}_4$  NPs homogeneously distributed; red curve:  $\text{Fe}_3\text{O}_4$  NPs self-assembled into a chain structure. Direction is approximately 50°.

an isotropic magnetic behavior along these three equivalent directions of symmetry. In particular, the magnetization curves display the same hysteretic and reversal behavior with coercive field ( $\mu_0 H_c$ ) of  $\approx 12.8$  mT and normalized remanent magnetization ( $M_r/M_{1.5T}$ ) of  $\approx 0.12$ . Conversely, the presence of chain-like

structures makes the magnetic response of the printed cube anisotropic, i.e., the magnetic properties depend on the relative direction of the applied magnetic field with respect to the major axis of the chains, see Figures 4c–e. In particular, when the magnetic field is applied along the major axis of the chains (i.e.,

the magnetic easy axis)—black curve in Figure 4c for the chains aligned along the  $x$ -direction and red curve in Figure 4d for the chains aligned along the  $y$ -direction—the hysteresis loops appear steeper with a faster approach to saturation than those obtained with the magnetic field applied in the other directions (i.e., magnetic hard axes). Instead, for the sample where the chains are at  $45^\circ$ , Figure 4e, the hysteresis loops measured along the  $x$  and  $y$  directions are now superimposed since, in this case, they are equivalent directions of symmetry with respect to the major axis of the chains. Of course, the magnetic response measured along these two equivalent directions is intermediate with respect to the ones measured along the magnetic easy and hard axes. The  $z$ -direction corresponds to the only magnetic hard axis, as confirmed by the slower approach to magnetic saturation. In all samples, as expected, a reduction of the  $H_c$  and  $M_r/M_{1.5T}$  values occurs from the easy axis to the hard one, insets in Figure 4c–e.

Cylindrical specimens with randomly distributed or oriented NPs were produced with the modified DLP 3D printer (example in Figure 4f). The polar plot of  $M_\perp$  measured for both randomly distributed (black curve) and self-assembled NPs (red curve) is reported in Figure 4g, showing the symmetry of the magnetic anisotropy induced by the microstructure of the magnetic filler. The approximately round shape of the black curve indicates an almost perfectly isotropic magnetic behavior for the sample containing randomly distributed NPs. Conversely, a two-lobe profile is observed in the sample containing magnetic chains (red curve), which is the fingerprint of the presence of a uniaxial anisotropy within the sample,<sup>[86]</sup> i.e., only one easy axis of magnetization originates from the elongated shape of the magnetic chains.

Using the magnetic susceptibility at the coercive field ( $\chi_c$ ) as a probing parameter, it is possible to determine the amount of magnetic fillers in the printed objects that maximizes the anisotropic magnetic response. The  $\chi_c$  values measured both parallel (full squares) and perpendicular (open circles) to the chains' major axis from the corresponding hysteresis loops are shown in Figure S2 (Supporting Information). The value of  $\chi_c$  corresponding to the randomly distributed NPs (gray dashed line) is used as reference. As expected, for all the concentrations of NPs up to 8 wt%, the parallel- $\chi_c$  values are systematically higher than the corresponding perpendicular- $\chi_c$  values indicating a magnetic anisotropic effect. However, the parallel- $\chi_c$  shows a nonmonotonic behavior, where an increase as a function of the concentration of magnetic NPs is observed up to 4 wt% at which a value of about  $20 \text{ T}^{-1}$  is reached. This value remains almost constant up to 6 wt%, and then decreases at 8 wt% to a value close to the one obtained for samples loaded with 0.5 wt% of NPs. On the other hand, the perpendicular- $\chi_c$  values remain almost constant at about  $8.5 \text{ T}^{-1}$  close to the reference value (gray dashed line) regardless of the concentration of fillers. Thus, two conclusions can be drawn: i) the magnitude of magnetic susceptibility in the direction of the magnetic anisotropy can be tuned by the amount of NPs loaded in the polymer, with an optimum concentration of the fillers in the range 4–6 wt%; ii) along the direction perpendicular to the chains' major axis, the effect of the anisotropy is weak. Moreover, the magnitude of the magnetic susceptibility in the directions perpendicular to the easy axis is almost independent on the NPs concentration

as it is observed that the magnetization reversal mechanism is very similar to that of uniformly dispersed NPs.

An estimate of the average chains' aspect ratio ( $\alpha$ ) and of the contribution to the effective magnetic anisotropy by the chain shape ( $K_s$ ) has been obtained by using the procedure described in the Supporting Information and is reported in Figure S3c (Supporting Information) for all  $\text{Fe}_3\text{O}_4$ -loaded printed samples. The value of  $\alpha$  shows a nonmonotonic behavior with a maximum value of about 1.8 for a NP concentration in the range 4–6 wt%. This suggests that an initial increase in NP concentration within the polymer composite leads to the formation of longer chains, in agreement with SEM observations and numerical simulations (see Figure 2) as well as existing literature.<sup>[62,87,88]</sup> On the other hand, the reduced value of  $\alpha$  observed for a load of 8 wt% can be explained by the fact that when the amount of embedded NPs overcomes a threshold value, the self-assembly process forms overlapping and interconnected magnetic chains (see Figure 2c2). Therefore, the chains no longer act as isolated magnetic units but as larger and interacting magnetic assemblies. This affects the overall magnetic behavior by reducing the contribution to the effective magnetic anisotropy, and in turn by decreasing the magnetic susceptibility of the composite material. In addition, the evolution of  $K_s$  values, also shown in Figure S3c (Supporting Information), has a similar trend to that of  $\alpha$  with a maximum value of about  $6.3 \times 10^3 \text{ J m}^{-3}$  in the range 4–6 wt% of embedded NPs, which thus represents the optimum load of magnetic fillers. These results show the effectiveness of the magnetic field-driven self-assembly process during the DLP printing step to program the effective magnetic anisotropy of the polymer composite, which in turn induces a net magnetic moment capable of yielding an actuation motion by magnetic torque.

We previously demonstrated that the mechanical properties (e.g., stiffness) of the printed composite can be tuned by varying the amount of BA in the Ebecryl (Eb) resin, and that the optimum concentration of fillers for the printing process under the application of a constant magnetic field of 10 mT is 6 wt%.<sup>[77,78]</sup> Here, the effect of the orientation of the chains on the mechanical properties of the printed materials was studied (Figure S4, Supporting Information). For the stiffer sample (75Eb25BA\_6NPs), the value of the elastic modulus is, within the error bar, equivalent to that of the reference sample, i.e.,  $E = 4.5 \text{ MPa}$ . Thus, the orientation of the microstructure does not alter the mechanical response of the composites when subjected to tensile stress. For the softer sample (50Eb50BA\_6NPs), a reduction of the elastic modulus of about 10% is observed with respect to the reference sample containing only dispersed NPs, i.e.,  $E = 3.75 \text{ MPa}$ . This is presumably due to the incorporation of larger aggregate-inducing defects, as already observed in soft samples.<sup>[77]</sup>

Once both the magnetic and mechanical properties of the 3D printed materials with oriented NPs were studied in detail, the information was subsequently employed to develop 3D printed objects with programmed response, and finally 3D printed magnetic devices, exploiting magnetic fields. Indeed, when a 3D printed device containing a magnetic microstructure is subjected to an external magnetic field, a magnetic torque ( $\tau_m$ ) is exerted on the extended magnetic dipole, which forces the chains to rotate in order to align their easy magnetic axis along

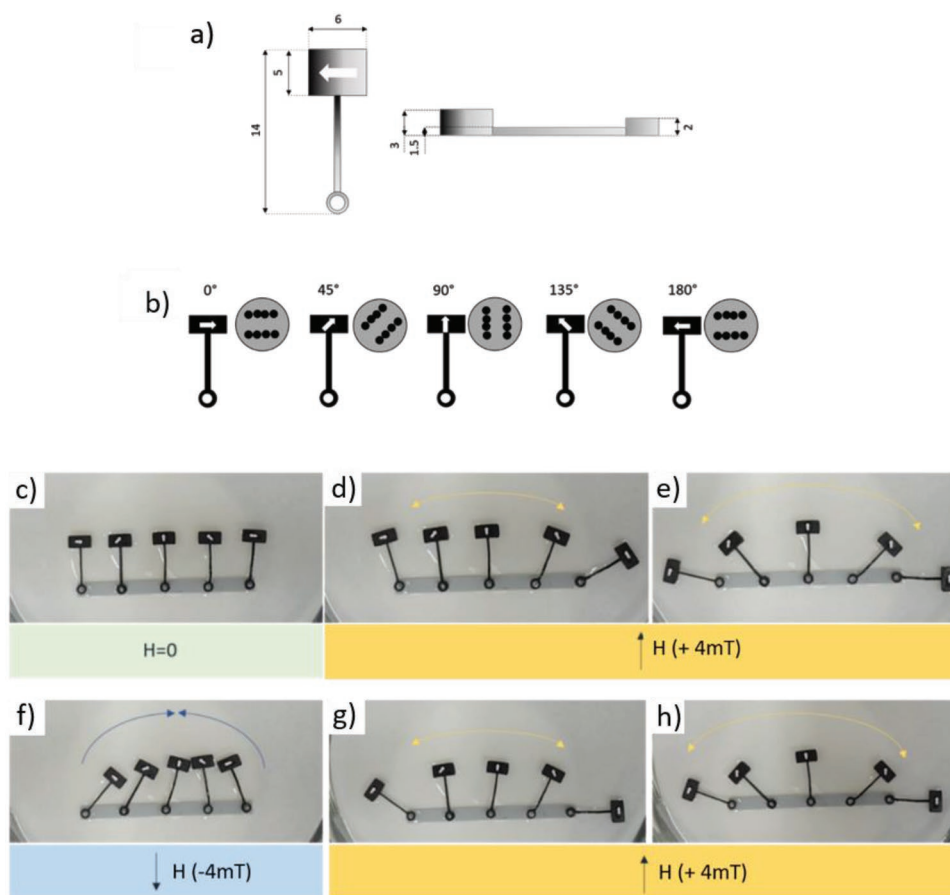


**Figure 5.** a) Dimensions of the 3D printed rigid magnetic hammers (mm) and b) orientation of the microstructure within each hammer. c–h) Time evolution of rigid magneto-responsive hammers having different orientations of the microstructure (indicated by the arrows) as a function of the applied magnetic field.

the field direction.<sup>[65,70,89–93]</sup> In general, the magnetic torque can be expressed as:  $\tau_m = dU_m/d\theta$ , where  $U_m$  is the magnetic energy of the material and  $\theta$  is the rotation angle. Approximating a chain to a prolate ellipsoid with  $a$  and  $b$  its long and short dimensions,  $U_m$  can be written as:<sup>[65]</sup>

$$U_m = \frac{2\pi ab^2}{3} \frac{\bar{\chi}^2}{\bar{\chi} + 2} \mu_0 H^2 \sin^2 \theta \quad (1)$$

where  $\bar{\chi} = 3\chi/\chi + 2$  is the shape-corrected susceptibility of the magnetic unit and  $H$  is the applied magnetic field. When the magnetic chains are confined within and anchored to the host polymeric matrix, the torque is transferred to the whole material. In this case, two pathways are possible: if the composite is rigid it will be subject to an overall rotation; conversely, if the composite is soft and the magnetic torque overcomes the mechanical resistance of the material, the object will deform.<sup>[65,70,93]</sup> Thus, using the modified DLP printer to control the microstructure during the printing process, as well as the initial formulation to tune the stiffness of the printed sample, several magnetically driven actuators have been obtained.

First, rigid hammer-like structures undergoing predefined rotations were obtained. The magneto-responsive hammers

were 3D printed using the 75Eb25BA formulation loaded with 6 wt% of NPs, 75Eb25BA\_6NPs (Figure 5a).

Five hammers were printed, each having a defined orientation of the microstructure, i.e., 0°, 45°, 90°, 135°, and 180° as indicated by the arrows in Figure 5b. To minimize the friction effects, the hammers were placed in a petri dish filled with water and each hammer was anchored to a pinion of a 3D printed rack. Their rotations were studied by using a pair of Helmholtz coils generating a magnetic field up to 4 mT in the  $x$ - $y$  plane, Figure S5 (Supporting Information).

In the initial configuration, the magnetic field is switched off ( $H = 0$ ) and all the hammers are parallel one to another as shown in Figure 5c. As soon as the field is applied ( $H = +4$  mT) in the direction indicated in Figure 5d, each hammer starts to rotate around its anchoring point until the equilibrium configuration is reached (Figure 5e). This is until the microstructure, indicated by the arrow, aligns with the direction of the applied field. As each hammer has a specific microstructure, they rotate at a different angle. By reversing the direction of the applied field ( $H = -4$  mT), it is possible to reverse the process, Figure 5f. Finally, the repeatability of the process is demonstrated by inverting again the direction of the applied field ( $H = +4$  mT) (Figure 5g–h). A complete sequence of the controlled motion of these actuators is reported in Video S1 (Supporting Information).

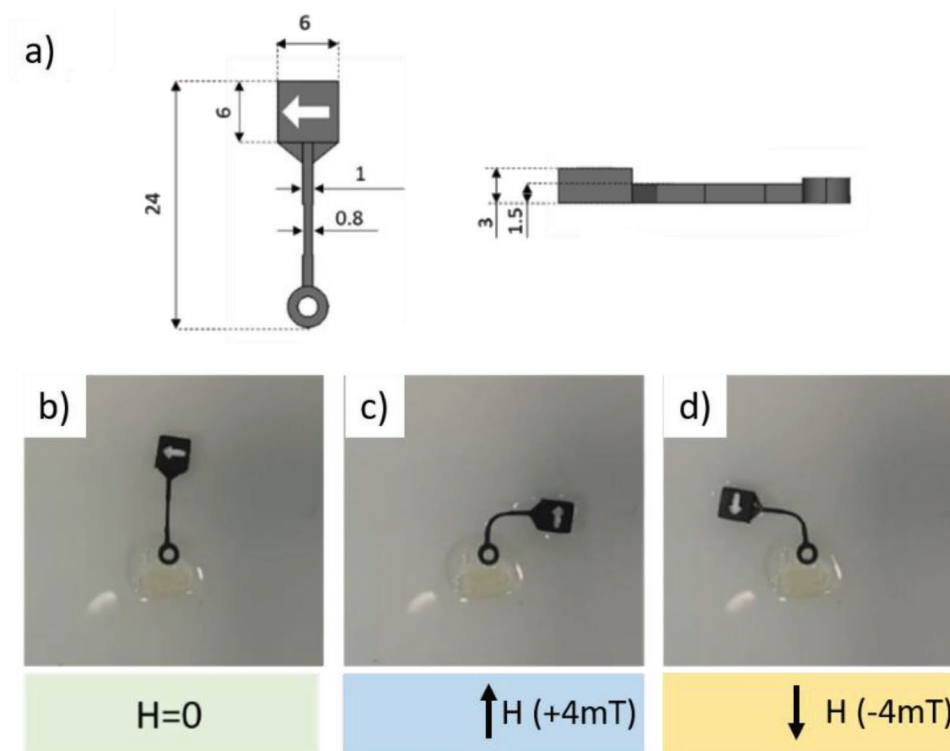


**Figure 6.** a) Design of a magneto-responsive soft hammer. The microstructure is indicated by the arrow on the head of the hammer. b) Initial configuration ( $H = 0$ ) and c–d) bending of the magneto-responsive soft hammer for two opposite directions of the applied magnetic field.

A similar approach was then used to exploit the bending of printed soft composites. In this case, the magnetic force ( $\tau_{\text{Magnetic}}$ ) must overcome the mechanical resistance of the material ( $\tau_{\text{Mechanic}}$ ) to obtain bending. Thus, magneto-responsive flexible actuators can be printed by either increasing the intensity of the applied magnetic field or by reducing the mechanical resistance of the sample. The latter option can be obtained either by tuning the stiffness of the matrix and/or by changing the geometry of the sample. In the present case, both the mechanical properties of the object and its design have been adapted. In particular, a soft hammer was printed using the 50Eb50BA formulation loaded with 6 wt% of NPs (50Eb50BA\_6NPs) and its mechanical resistance was decreased by locally reducing the thickness of the hammer's arm as indicated in **Figure 6a**. Again, friction effects have been minimized by placing the hammer in a petri dish filled with water. Contrarily to the rigid hammers, the extremity of the flexible hammer was fixed to a support for preventing the object to rotate. As the bending of a millimeter-size actuator necessitates an intensity of the magnetic field larger than the one that can be obtained using standard Helmholtz coils, a couple of NdFeB permanent magnets have been used to activate the actuation process as described in Supporting Information. The initial configuration ( $H = 0$ ) is shown in **Figure 6b**, where the orientation of the microstructure is indicated by the arrow. A magnetic field is then applied normally to the microstructure, whose magnitude was tuned by an Arduino controller by varying the relative distance between a couple of magnets. Below a critical distance the magnetic torque ( $\tau_{\text{mag}}$ ) overcomes the mechanical one

( $\tau_{\text{mech}}$ ) and the hammer starts bending to realign its easy magnetic axis in the direction of the field (**Figure 6c**). As expected, when reversing the polarity of the magnets, the bending is observed in the opposite direction (**Figure 6d**). The complete sequence of the bending of the hammer is reported in Video S2 (Supporting Information).

To increase the degree of complexity on our objects, the possibility to 3D print magnetically driven gears is checked. Mechanical gears are toothed wheels that transmit rotation and power from one shaft to another, or that work in combination with one or more other gears to alter the relationship between the speeds of the driver and the driven parts. Magnetic gears, first patented by Armstrong in 1901,<sup>[94]</sup> resemble the traditional mechanical gears in geometry and function, except that the force/torque transmission exerted by tooth meshing is replaced with the contactless magnetic interaction. As two opposing magnets approach each other, they repel; when placed on two rings the magnets will act like teeth.

First, the feasibility of remote control of gear rotation has been verified by printing two identical elements, i.e., using the same formulation (75Eb25BA\_6NPs) and the same design (10 teeth, 1 mm module, and a pressure angle of  $20^\circ$ ), but with different microstructures (oriented and dispersed NPs) as reported in **Figure S6** (Supporting Information). The reversibility of the process has been checked by switching the magnetic field several times. The complete sequence is reported in **Figure S6** (Supporting Information) and in **Video S3** (Supporting Information). The interpretation of these experimental results is quite straightforward, and it is clearly related to the different microstructures

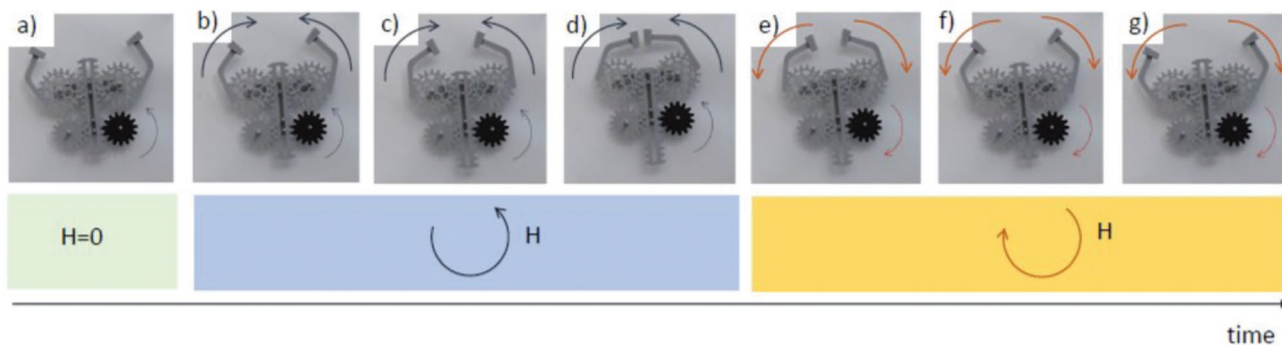


**Figure 7.** a–g) Timeframe evolution of the magnetically driven clamp driven by a magnetoactive drive gear.

of the two objects. On one hand, a sample containing dispersed NPs is magnetically isotropic as indicated by the hysteresis cycles (Figure 4b), thus the application of a uniform magnetic field does not generate a net magnetic torque, and the rotation of the sample is nearly absent. On the other hand, the presence of a microstructure in the sample creates a magnetic anisotropy in the object, which in turn generates a magnetic torque ( $\approx M_{\text{easy}} \times H$ ) forcing the gear to rotate.

When two or more gears are linked together, the ensemble is considered as a gear train where the “input gear” (also known as drive gear) transmits the power to the “output gear” (also known as driven gear), Figure S7 (Supporting Information). In a standard gear train, the input gear is typically connected to a power source, such as a DC motor. In this case, the magnetoactive drive gear is remotely controlled by an external magnetic field, and the driven gear is nonmagnetic and printed using an inert resin. The complete sequence of work is reported in the Supporting Information of this manuscript (Figure S7 and Video S4, Supporting Information).

A further step was to fabricate a linear actuator composed of a spur gear and a linear rack coupled together through the meshing of their respective teeth. The complete sequence as well as the explanation of the process is reported in the Supporting Information of this manuscript (Figure S8, Supporting Information).

The linear actuator was then employed to build a magnetic driven gripper. Generally speaking, grasping is the ability to pick up and hold an object, while manipulation is the ability to produce rotation and displacement. Grasping and manipulation are two functions that are of paramount importance in robotics as they allow the machine to mimic the behavior of human beings and animals. This device is composed of two nonmagnetic clamping arms activated by a magnetoactive linear actuator. In the literature, some magnetically driven grippers have been reported, but they are based on the 3D printing of magnetic composites.<sup>[95,96]</sup> In contrast, in the present case, the magnetic component was decoupled from the gripping part, allowing remote control without the necessity to insert magnets close to the gripping part, but instead exploiting the programmed microstructure of the gears. The operation of this magnetoactive gripper is illustrated in Figure 7a–g. In the initial configuration, the two arms of the grippers are in the open position, i.e., they are far from each other. When the magnetic field is switched on, the magnetoactive drive gear

starts to rotate anticlockwise, transferring its motion to the rack. Then, a couple of driven gears transform again the translating motion of the rack into a rotary one. As they have been printed with an arm and a clamp, they play the role of the hands of the gripper. Inverting the field allows the magnetoactive spur gear to rotate clockwise, and the arms of the gripper to open up and return to their initial configuration. The complete sequence is reported in the Supporting Information of this manuscript (Video S5, Supporting Information). This proof-of-concept example indicates that the development of magnetoactive devices with advanced functionalities is technically possible.

### 3. Conclusion

Magnetoactive polymers with oriented microstructures behave as magnetic compasses. Indeed, when a uniform magnetic field is applied, the composite sample undergoes rotation movements (if rigid) or bending (if soft) to align its easy magnetic axis along the field lines. Taking advantage of this phenomenon, we printed magnetically driven macroscopic elements undergoing programmed movements by the remote application of a magnetic field. Our approach is based on the ability to tune the self-assembly of the magnetic microstructure ( $\text{Fe}_3\text{O}_4$ ) and to control its orientation in a photocurable resin during the printing process thanks to the modification of a DLP-type printer.

In this work, our approach is first applied to fabricate magnetoactive hammer-like actuators with different stiffnesses allowing both pure rotation or/and bending motions. As an application, these elements could be used to create a magnetoactive electric-switch. Then, by introducing the idea that the microstructure can be exploited to create a magnetoactive gear, we showed that the latter can be successfully used to transfer torque to other gears, thereby converting a rotation movement into linear translation. Finally, we demonstrated that magnetoactive gears can be also combined with other nonmagnetic elements to create complex assemblies, such as gear-trains, linear actuators, and grippers that can be remotely controlled. We believe that our approach can be further developed to achieve even more complex component systems and could generate new opportunities in robotics-related applications.

## 4. Experimental Section

**Formulation:** The magnetoactive formulation was obtained by adding magnetite NPs ( $\text{Fe}_3\text{O}_4$  NPs, 50–100 nm diameter) to a photocurable Urethane Acrylate resin (Ebecryl 8232) with different amount of BA and using phenylbis(2,4,6-trimethylbenzoyl)phosphine oxide (Merck) as the photoinitiator (1 wt% of the monomers), as reported by Lantean et al.<sup>[77]</sup> As demonstrated in this work, this last ingredient was used both to adjust the viscosity of the formulation and to control the mechanical properties. In particular, three different weight concentrations of BA had been considered (0%, 25%, and 50%), leading to three different formulations, hereafter named as 100Eb, 75Eb25BA, and 50Eb50BA. Their corresponding viscosity has been measured to be  $\eta = 5.6$  Pa s,  $\eta = 1.8$  Pa s, and  $\eta = 0.02$  Pa s. Spherical shape magnetite ( $\text{Fe}_3\text{O}_4$ ) NPs with a nominal diameter ranging between 50 and 100 nm (98% purity) were purchased from Merck and used as received. NPs were dispersed in the formulation by stirring followed by sonication, following previously reported procedures.<sup>[77]</sup> Viscosity and photoreactivity of the formulations had been used to tune both the mechanical properties of the printed object as well as the dimensions of the embedded chain-like aggregates of  $\text{Fe}_3\text{O}_4$  NPs, as already reported by Lantean et al.<sup>[78]</sup>

**Self-Assembly Driven Magnetic Microstructure:** The average length of the self-assembled chains, their spatial orientation, and the concentration of the loaded magnetic fillers have been studied in situ using a Leica DFC295 optical microscope equipped with a 10 $\times$  optics, and experimental results have been rationalized by using numerical simulations based on a dipolar approximation model.<sup>[78,97,98]</sup> The viscosity effect has been investigated for the 75Eb25BA and 50Eb50BA formulations by coating, with the help of a wire wound bar, a 200  $\mu\text{m}$  thick film on the surface of a microscope slide. This thickness has been chosen to mimic 10 layers (20  $\mu\text{m}$  each) of a printed sample.

The orientation step is triggered by applying a 10 mT magnetic field in the horizontal direction ( $\theta_B = 0$ ), with an initial waiting time of 180 s, to let the chains reach stable dimension. Those parameters were based on a previous study of Lantean et al.<sup>[77]</sup> Then, the magnetic field is rotated by  $\theta_B = 30^\circ$  and the image taken 120 s after the rotation step. Experimental results have been coupled to numerical simulations on a system composed of 1000 NPs using periodic boundary conditions.<sup>[78,79]</sup> The size of the cubic box depends on the weight fraction of NPs. More details can be found in the Supporting Information File.

**DLP Printer Modification and Printing Parameters:** The control of the microstructure within the printed composite polymers is obtained by using a modified DLP machine (RobotFactory HD 2.0+) as described in a previous work.<sup>[77]</sup> As shown in Figure 1a,b, a linear-to-rotary actuator driven by an Arduino microcontroller is used to control the rotation of a nonmagnetic ball-bearing glued on the bottom glass plate of the vat. Its role is twofold: i) the central hole acts as a resin reservoir, while ii) the rotating external wall is used to apply the magnetic field in the X–Y plane (H) by fixing to it two permanent magnets of suitable intensity. The intensity of the applied magnetic field has been tested by considering several combinations of permanent magnets, hereafter named as A and B (www.supermagnete.fr). The A magnet is a  $60 \times 10 \times 2$  mm<sup>3</sup> parallelepiped exhibiting a magnetic field at the surface of 120 mT, while the B magnet is a  $40 \times 10 \times 5$  mm<sup>3</sup> parallelepiped exhibiting a magnetic field at the surface of 310 mT. Finally, to fit with the new resin reservoir, the original building platform was modified by adding an appropriately sized glass cylinder.

The processing parameters have been determined for 75Eb25BA and 50Eb50BA formulations by printing rectangular samples (3 mm thick) for increasing concentration of  $\text{Fe}_3\text{O}_4$  NPs (up to 8 wt%) in the absence and presence of magnetic field, i.e.,  $B = 0$  mT and  $B = 10$  mT, respectively. The thickness of each printed layer was set to be 20  $\mu\text{m}$ . Table 1 reports the processing parameters for the different formulations. All the different structures tested along the manuscript were 3D printed following these parameters. For the samples with oriented nanochains, before printing, a waiting time of 180 s was fixed to allow the formation of the chains in the printable formulations.

**Characterization:** The dispersion of magnetic fillers as well as their self-assembly in chains was investigated by using a Zeiss Supra 40 Field Emission Scanning Electron Microscopy (FESEM). Cryo-fracturing of photocured samples was used to avoid plastic deformation and filamentary aggregates.

The magnetic properties of the 3D printed objects have been investigated at room temperature by an alternating gradient field magnetometer (AGFM) operating with an applied magnetic field in the range  $-1.5$  T up to  $+1.5$  T. The hysteresis loops (i.e., the magnetization vs. applied magnetic field curves,  $M(H)$ ) have been measured along the three symmetry equivalent directions—hereafter named as parallel ( $x$ -direction), transverse ( $y$ -direction), and perpendicular ( $z$ -direction) of a 3D printed cubic sample ( $3 \times 3 \times 3$  mm<sup>3</sup>). All magnetic curves have been normalized to the magnetic moment value at  $H = 1.5$  T.

The hysteresis curve allows to evaluate the magnetic susceptibility,  $\chi$ , which is defined by  $\chi = M/H$ . It describes the way in which  $M$  varies within the material as a function of the applied field  $H$ . As  $\chi$  is a tensor, it can be used to estimate the magnetic behavior of the sample along different spatial directions. Here, the magnetic susceptibility measured at the coercive field of the hysteresis curve  $\chi_c(H_c)$  has been selected as a physical indicator to estimate the degree of magnetic anisotropy in the sample.

Two microstructural configurations of printed samples loaded with 6 wt% of  $\text{Fe}_3\text{O}_4$  NPs have been investigated: i) randomly distributed NPs, and ii) self-assembled chains. For the latter, chains are created before the additive step by applying a magnetic field of 10 mT in the  $x$ – $y$  plane along three different directions,  $0^\circ$ ,  $45^\circ$ , or  $90^\circ$  with respect to the  $x$ -direction.

Vector-vibrating sample magnetometer (V-VSM) was used to study the angular dependence of the magnetic anisotropy in both samples. In particular, the component of magnetization ( $M_\perp$ ) perpendicular to the direction of the applied magnetic field was measured as a function of the angle during the relative rotation of the sample. To this end, samples with both randomly and filamentary distributed NPs were 3D printed with a cylindrical shape to avoid any magnetic anisotropy effect.

Dynamic mechanical thermal analysis (DMTA) in tensile configuration (Triton Technology TTDMA equipment) was used to measure mechanical properties. Elongation tests were run at room temperature in load control ( $1$  N  $\text{min}^{-1}$ ). The dimensions of the tested specimens are  $30 \times 4 \times 3$  mm<sup>3</sup> (length  $\times$  width  $\times$  thickness) with chains oriented at  $0^\circ$ ,  $45^\circ$ , and  $90^\circ$  relative to the length of the sample. For comparison, 3D printed samples with randomly dispersed NPs are used as reference.

3D scanning of the 3D printed object was performed with a E3 scanner (3shape). The comparison heat map was obtained by the Convince software (3shape).

## Supporting Information

Supporting Information is available from the Wiley Online Library or from the author.

## Acknowledgements

This work was supported by Compagnia di San Paolo through the “Joint Project with Top Universities” grant. This work has benefited from the financial support of the LabEx LaSIPS (ANR-10-LABX-0032-LaSIPS) managed by the French National Research Agency under the “Investissements d’avenir” program (ANR-11-IDEX-0003-02). This work was also performed using HPC resources from École Polytechnique through the LLR-LSI project and from the “Mésocentre” computing center of CentraleSupélec and École Normale Supérieure Paris-Saclay supported by CNRS and Région Île-de-France (<http://mesocentre.centralesupelec.fr/>).

Open access funding provided by Politecnico di Torino within the CRUI-CARE Agreement.

## Conflict of Interest

The authors declare no conflict of interest.

## Authors Contribution

S.L. conducted the investigations and helped in the preparation of the first draft of the paper. I.R. and G.R. designed the research and supervised the results and data analysis, preparing the first draft of the paper. M.S., L.B. and C.F.P. performed data analysis and discussion of the results. M.H. and H.D. performed simulations. G.B. and P.T. performed magnetic characterization and analysis. All the authors contributed in writing and revised the paper.

## Data Availability Statement

The data that support the findings of this study are available in the supplementary material of this article.

## Keywords

4D printing, magnetic devices, programmed microstructures, magnetic actuation

Received: February 22, 2022  
Revised: May 10, 2022  
Published online: June 17, 2022

- [1] P. Fratzl, R. Weinkamer, *Prog. Mater. Sci.* **2007**, *52*, 1263.  
[2] P. Fratzl, *J. R. Soc., Interface* **2007**, *4*, 637.  
[3] J. C. Weaver, G. W. Milliron, A. Miserez, K. Evans-Lutterodt, S. Herrera, I. Gallana, W. J. Mershon, B. Swanson, P. Zavattieri, E. DiMasi, D. Kisailus, *Science* **2012**, *336*, 1275.  
[4] L. K. Grunenfelder, N. Suksangpanya, C. Salinas, G. Milliron, N. Yaraghi, S. Herrera, K. Evans-Lutterodt, S. R. Nutt, P. Zavattieri, D. Kisailus, *Acta Biomater.* **2014**, *10*, 3997.  
[5] A. M. C. Emons, B. M. Mulder, *Trends Plant Sci.* **2000**, *5*, 35.  
[6] I. Burgert, P. Fratzl, *Integr. Comp. Biol.* **2009**, *49*, 69.  
[7] A. Fabricant, G. Z. Iwata, S. Scherzer, L. Bougas, K. Rolfs, A. Jodko-Władzińska, J. Voigt, R. Hedrich, D. Budker, *Sci. Rep.* **2021**, *11*, 1438.  
[8] R. Sachse, A. Westermeier, M. Mylo, J. Nadasdi, M. Bischoff, T. Speck, S. Poppinga, *Proc. Natl. Acad. Sci. USA* **2020**, *117*, 16035.  
[9] A. L. Duigou, M. Castro, *Ind. Crops Prod.* **2017**, *99*, 142.  
[10] A. Scheffel, M. Gruska, D. Favier, A. Linaourodos, J. M. Plitzko, D. Schüler, *Nature* **2006**, *440*, 110.  
[11] S. Tibbits, *Archit. Des.* **2014**, *84*, 116.  
[12] Z. X. Khoo, J. E. M. Teoh, Y. Liu, C. K. Chua, S. Yang, J. An, K. F. Leong, W. Y. Yeong, *Virtual Phys. Prototyping* **2015**, *10*, 103.  
[13] A. Mitchell, U. Lafont, M. Holyńska, C. Semprinoschnig, *Addit. Manuf.* **2018**, *24*, 606.  
[14] D. G. Shin, T. H. Kim, D. E. Kim, *Int. J. Precis. Eng. Manuf. – Green Technol.* **2017**, *4*, 349.  
[15] S. E. Bakarich, R. Gorkin, M. I. H. Panhuis, G. M. Spinks, *Macromol. Rapid Commun.* **2015**, *36*, 1211.  
[16] Y. Hu, Z. Wang, D. Jin, C. Zhang, R. Sun, Z. Li, K. Hu, J. Ni, Z. Cai, D. Pan, X. Wang, W. Zhu, J. Li, D. Wu, L. Zhang, J. Chu, *Adv. Funct. Mater.* **2020**, *30*, 1907377.  
[17] J. Guo, R. Zhang, L. Zhang, X. Cao, *ACS Macro Lett.* **2018**, *7*, 442.  
[18] M. N. I. Shiblee, K. Ahmed, M. Kawakami, H. Furukawa, *Adv. Mater. Technol.* **2019**, *4*, 1900071.  
[19] L. H. Shao, B. Zhao, Q. Zhang, Y. Xing, K. Zhang, *Extreme Mech. Lett.* **2020**, *39*, 100793.  
[20] D. Grinberg, S. Siddique, M. Q. Le, R. Liang, J. F. Capsal, P. J. Cottinet, *J. Polym. Sci., Part B: Polym. Phys.* **2019**, *57*, 109.  
[21] T. Mirfakhrai, J. D. W. Madden, R. H. Baughman, *Mater. Today* **2007**, *10*, 30.  
[22] H. Meng, G. Li, *Polymer* **2013**, *54*, 2199.  
[23] J. Wu, C. Yuan, Z. Ding, M. Isakov, Y. Mao, T. Wang, M. L. Dunn, H. J. Qi, *Sci. Rep.* **2016**, *6*, 24224.  
[24] K. Yu, A. Ritchie, Y. Mao, M. L. Dunn, H. J. Qi, *Procedia IUTAM* **2015**, *12*, 193.  
[25] Y. Mao, K. Yu, M. S. Isakov, J. Wu, M. L. Dunn, H. Jerry Qi, *Sci. Rep.* **2015**, *5*, 13616.  
[26] M. Zarek, M. Layani, I. Cooperstein, E. Sachyani, D. Cohn, S. Magdassi, *Adv. Mater.* **2016**, *28*, 4449.  
[27] A. Muzaffar, M. B. Ahamed, K. Deshmukh, T. Kovářik, T. Křenek, S. K. Pasha, in *3D and 4D Printing of Polymer Nanocomposite Materials: Processing, Applications, and Challenges*, (Eds: K. K. Sadasivuni, K. Deshmukh, M. A. Almaadeed), Elsevier **2019**, p. 85.  
[28] X. Zhang, P. Yang, Y. Dai, P. Ma, X. Li, Z. Cheng, Z. Hou, X. Kang, C. Li, J. Lin, *Adv. Funct. Mater.* **2013**, *23*, 4067.  
[29] H. Yang, W. R. Leow, T. Wang, J. Wang, J. Yu, K. He, D. Qi, C. Wan, X. Chen, *Adv. Mater.* **2017**, *29*, 1701627.  
[30] I. Roppolo, A. Chiappone, A. Angelini, S. Stassi, F. Frascella, C. F. Pirri, C. Ricciardi, E. Descrovi, *Mater. Horiz.* **2017**, *4*, 396.  
[31] L. Ren, X. Zhou, Q. Liu, Y. Liang, Z. Song, B. Zhang, B. Li, *J. Mater. Sci.* **2018**, *53*, 14274.  
[32] J. J. Martin, B. E. Fiore, R. M. Erb, *Nat. Commun.* **2015**, *6*, 8641.  
[33] Z. Jia, Y. Yu, S. Hou, L. Wang, *J. Mech. Phys. Solids* **2019**, *125*, 178.  
[34] Y. Yang, X. Li, M. Chu, H. Sun, J. Jin, K. Yu, Q. Wang, Q. Zhou, Y. Chen, *Sci. Adv.* **2019**, *5*, eaau9490.  
[35] B. Wang, T. N. Sullivan, A. Pissarenko, A. Zaheri, H. D. Espinosa, M. A. Meyers, *Adv. Mater.* **2019**, *31*, 1804574.  
[36] L. Zorzetto, D. Ruffoni, *Adv. Funct. Mater.* **2019**, *29*, 1805888.  
[37] M. Peng, Z. Wen, L. Xie, J. Cheng, Z. Jia, D. Shi, H. Zeng, B. Zhao, Z. Liang, T. Li, L. Jiang, *Adv. Mater.* **2019**, *31*, 1902930.  
[38] S. M. Sajadi, P. S. Owuor, S. Schara, C. F. Woellner, V. Rodrigues, R. Vajtai, J. Lou, D. S. Galvão, C. S. Tiwary, P. M. Ajayan, *Adv. Mater.* **2018**, *30*, 1704820.  
[39] L. Ren, B. Li, Z. Song, Q. Liu, L. Ren, X. Zhou, *Int. J. Precis. Eng. Manuf. – Green Technol.* **2019**, *6*, 89.  
[40] J. R. Raney, B. G. Compton, J. Mueller, T. J. Ober, K. Shea, J. A. Lewis, *Proc. Natl. Acad. Sci. USA* **2018**, *115*, 1198.  
[41] H. Arslan, A. Nojoomi, J. Jeon, K. Yum, *Adv. Sci.* **2019**, *6*, 1800703.  
[42] J. Liu, O. Erol, A. Pantula, W. Liu, Z. Jiang, K. Kobayashi, D. Chatterjee, N. Hibino, L. H. Romer, S. H. Kang, T. D. Nguyen, D. H. Gracias, *ACS Appl. Mater. Interfaces* **2019**, *11*, 8492.  
[43] A. Nojoomi, H. Arslan, K. Lee, K. Yum, *Nat. Commun.* **2018**, *9*, 3705.  
[44] M. Schaffner, J. A. Faber, L. Pianegonda, P. A. Rühls, F. Coulter, A. R. Studart, *Nat. Commun.* **2018**, *9*, 878.  
[45] Y. Hu, A. Xu, J. Liu, L. Yang, L. Chang, M. Huang, W. Gu, G. Wu, P. Lu, W. Chen, Y. Wu, *Adv. Mater. Technol.* **2019**, *4*, 1800674.  
[46] S. Ma, M. Scaraggi, C. Yan, X. Wang, S. N. Gorb, D. Dini, F. Zhou, *Small* **2019**, *4*, 1802931.  
[47] N. Bira, P. Dhagat, J. R. Davidson, *Front. Rob. AI* **2020**, *7*, 146.  
[48] K. J. Merazzo, A. C. Lima, M. Rincó N-Iglesias, L. C. Fernandes, N. Pereira, S. Lanceros-Mendez, P. Martins, *Mater. Horiz.* **2021**, *8*, 2654.  
[49] S. Malley, S. Newacheck, G. Youssef, *Addit. Manuf.* **2021**, *47*, 102239.  
[50] F. Qiu, B. J. Nelson, *Engineering* **2015**, *1*, 21.  
[51] H. Ceylan, J. Giltinan, K. Kozielski, M. Sitti, *Lab Chip* **2017**, *17*, 1705.  
[52] B. Nagarajan, P. Mertiny, A. J. Qureshi, *Mater. Today Commun.* **2020**, *25*, 101520.  
[53] Y. Zhang, Q. Wang, S. Yi, Z. Lin, C. Wang, Z. Chen, L. Jiang, *ACS Appl. Mater. Interfaces* **2021**, *13*, 4174.

- [54] S. Lucarini, M. Hossain, D. Garcia-Gonzalez, *Compos. Struct.* **2022**, 279, 114800.
- [55] Y. Kim, H. Yuk, R. Zhao, S. A. Chester, X. Zhao, *Nature* **2018**, 558, 274.
- [56] M. Gastaldi, F. Cardano, M. Zanetti, G. Viscardi, C. Barolo, S. Bordiga, S. Magdassi, A. Fin, I. Roppolo, *ACS Mater. Lett.* **2021**, 3, 1.
- [57] M. Xie, W. Zhang, C. Fan, C. Wu, Q. Feng, J. Wu, Y. Li, R. Gao, Z. Li, Q. Wang, Y. Cheng, B. He, *Adv. Mater.* **2020**, 32, 2000366.
- [58] H. Song, H. Lee, J. Lee, J. K. Choe, S. Lee, J. Y. Yi, S. Park, J.-W. Yoo, M. S. Kwon, J. Kim, *Nano Lett.* **2020**, 20, 5185.
- [59] J. Zhang, Y. Wang, H. Pang, S. Sun, Z. Xu, L. Shen, X. Cao, C. Sun, B. Wang, X. Gong, *Composites, Part A* **2021**, 150, 106591.
- [60] A. A. Kuznetsov, *J. Magn. Magn. Mater.* **2019**, 470, 28.
- [61] W. Zhang, P. K. J. Wong, D. Zhang, J. Yue, Z. Kou, G. van der Laan, A. Scholl, J. G. Zheng, Z. Lu, Y. Zhai, *Adv. Funct. Mater.* **2017**, 27, 1701265.
- [62] Y. Zhang, L. Sun, Y. Fu, Z. C. Huang, X. J. Bai, Y. Zhai, J. Du, H. R. Zhai, *J. Phys. Chem. C* **2009**, 113, 8152.
- [63] Y. I. Dikansky, D. V. Gladkikh, A. A. Zakinyan, A. G. Ispiryanyan, A. R. Zakinyan, *J. Mol. Liq.* **2020**, 319, 114171.
- [64] D. Lisjak, A. Mertelj, *Prog. Mater. Sci.* **2018**, 95, 286.
- [65] R. M. Erb, J. J. Martin, R. Soheilani, C. Pan, J. R. Barber, *Adv. Funct. Mater.* **2016**, 26, 3859.
- [66] L. Zhang, J. J. Abbott, L. Dong, B. E. Kratochvil, D. Bell, B. J. Nelson, *Appl. Phys. Lett.* **2009**, 94, 064107.
- [67] R. M. Erb, J. S. Sander, R. Grisch, A. R. Studart, *Nat. Commun.* **2013**, 4, 1712.
- [68] S. R. Mishra, M. D. Dickey, O. D. Velev, J. B. Tracy, *Nanoscale* **2016**, 8, 1309.
- [69] A. Crivaro, R. Sheridan, M. Frecker, T. W. Simpson, P. Von Lockette, *J. Intell. Mater. Syst. Struct.* **2016**, 27, 2049.
- [70] J. Kim, S. E. Chung, S. E. Choi, H. Lee, J. Kim, S. Kwon, *Nat. Mater.* **2011**, 10, 747.
- [71] H. Ceylan, I. C. Yasa, O. Yasa, A. F. Tabak, J. Giltinan, M. Sitti, *ACS Nano* **2019**, 13, 3353.
- [72] C. Peters, O. Ergeneman, P. D. W. Garcia, M. Müller, S. Pané, B. J. Nelson, C. Hierold, *Adv. Funct. Mater.* **2014**, 24, 5269.
- [73] Y. W. Lee, H. Ceylan, I. C. Yasa, U. Kilic, M. Sitti, *ACS Appl. Mater. Interfaces* **2021**, 13, 12759.
- [74] H. C. M. Sun, P. Liao, T. Wei, L. Zhang, D. Sun, *Micromachines* **2020**, 11, 404.
- [75] J. Giltinan, V. Sridhar, U. Bozuyuk, D. Sheehan, M. Sitti, *Adv. Intell. Syst.* **2021**, 3, 2000204.
- [76] R. Tognato, A. R. Armiento, V. Bonfrate, R. Levato, J. Malda, M. Alini, D. Eglin, G. Giancane, T. Serra, *Adv. Funct. Mater.* **2019**, 29, 1804647.
- [77] S. Lantean, G. Barrera, C. F. Pirri, P. Tiberto, M. Sangermano, I. Roppolo, G. Rizza, *Adv. Mater. Technol.* **2019**, 29, 1900505.
- [78] S. Lantean, I. Roppolo, M. Sangermano, M. Hayoun, H. Dammak, G. Rizza, *Addit. Manuf.* **2021**, 47, 102343.
- [79] I. S. Novikau, P. A. Sánchez, S. S. Kantorovich, *J. Mol. Liq.* **2020**, 307, 112902.
- [80] Y. Men, W. Wang, P. Xiao, J. G. Y. Men, W. Wang, P. Xiao, J. Gu, A. Sun, Y. Huang, J. Zhang, T. Chen, *RSC Adv.* **2015**, 5, 31519.
- [81] B. M. Smirnov, E. E. Son, D. V. Tereshonok, *J. Exp. Theor. Phys.* **2017**, 125, 906.
- [82] M. A. M. Gijs, *Microfluid. Nanofluid.* **2004**, 1, 22.
- [83] N. Pamme, *Lab Chip* **2006**, 6, 24.
- [84] N. A. Spaldin, *Magnetic Materials: Fundamentals and Applications*, Cambridge University Press, Cambridge **2010**.
- [85] V. S. Andreev, A. E. Luk'yanov, *Colloid J. USSR* **1990**, 51, 643.
- [86] Q. Wu, W. He, H. L. Liu, J. Ye, X. Q. Zhang, H. T. Yang, Z. Y. Chen, Z. H. Cheng, *Sci. Rep.* **2013**, 3, 1547.
- [87] M. Varón, M. Beleggia, T. Kasama, R. J. Harrison, R. E. Dunin-Borkowski, V. F. Puentes, C. Frandsen, *Sci. Rep.* **2013**, 3, 1234.
- [88] B. D. Cullity, C. D. Graham, *Introduction to Magnetic Materials*, 2nd ed., Wiley, Hoboken, NJ **2008**, <https://doi.org/10.1002/9780470386323>.
- [89] Z. Li, F. Yang, Y. Yin, *Adv. Funct. Mater.* **2020**, 30, 1903467.
- [90] P. Von Lockette, in *ASME 2014 Conf. Smart Materials, Adaptive Structures and Intelligent Systems (SMASIS) 2014*, Newport, Rhode Island, USA **2014**. <https://doi.org/10.1115/SMASIS20147590>.
- [91] H. W. Huang, M. S. Sakar, A. J. Petruska, S. Pané, B. J. Nelson, *Nat. Commun.* **2016**, 7, 12263.
- [92] T. Li, J. Li, K. I. Morozov, Z. Wu, T. Xu, I. Rozen, A. M. Leshansky, L. Li, J. Wang, *Nano Lett.* **2017**, 17, 5092.
- [93] L. Bodelot, J. P. Voropaieff, T. Pössinger, *Exp. Mech.* **2018**, 58, 207.
- [94] C. G. Armstrong, **1900**, US671330A.
- [95] Z. Ji, C. Yan, B. Yu, X. Wang, F. Zhou, *Adv. Mater. Interfaces* **2017**, 4, 1700629.
- [96] X. Cao, S. Xuan, S. Sun, Z. Xu, J. Li, X. Gong, *ACS Appl. Mater. Interfaces* **2021**, 13, 30127.
- [97] C. H. Bennett, *Diffusion in Solids: Recent Developments*, Elsevier Science, St. Louis, MO **1975**.
- [98] J. R. Beeler, R. E. Dahl Jr., R. D. Bourquin, *J. Phys. Colloq.* **1975**, 36, C4-97.